

# Domain-aligned generative downscaling enhances projections of extreme climate events

Ruian Tie<sup>1,4,5†</sup>, Xiaohui Zhong<sup>1,5†</sup>, Zhengyu Shi<sup>1,5†</sup>, Hao Li<sup>1,4,5\*</sup>,  
Jun Liu<sup>1,5</sup>, Wu Libo<sup>2,3,4,5\*</sup>

<sup>1</sup>Artificial Intelligence Innovation and Incubation Institute, Fudan University, 220 Handan Road, Shanghai, 200433, Shanghai, China.

<sup>2</sup>Institute for Big Data, Fudan University, 220 Handan Road, Shanghai, 200433, Shanghai, China.

<sup>3</sup>MOE Laboratory for National Development and Intelligent Governance, Fudan University, 220 Handan Road, Shanghai, 200433, Shanghai, China.

<sup>4</sup>Shanghai Innovation Institute, 669-3 Huafa Road, Shanghai, 200433, Shanghai, China.

<sup>5</sup>Shanghai Academy of AI for Science, 18-X3 Longyao Road, Shanghai, 200433, Shanghai, China.

\*Corresponding author(s). E-mail(s): [lihao\\_lh@fudan.edu.cn](mailto:lihao_lh@fudan.edu.cn);  
[wulibo@fudan.edu.cn](mailto:wulibo@fudan.edu.cn);

Contributing authors: [ratie25@m.fudan.edu.cn](mailto:ratie25@m.fudan.edu.cn); [x7zhong@gmail.com](mailto:x7zhong@gmail.com);  
[zhengyushi@fudan.edu.cn](mailto:zhengyushi@fudan.edu.cn); [23110240031@m.fudan.edu.cn](mailto:23110240031@m.fudan.edu.cn);

<sup>†</sup>These authors contributed equally to this work.

## Abstract

Climate change is exacerbating extreme weather events globally, including high temperatures, extreme precipitation, strong winds, and tropical cyclones, posing severe threats to human health, infrastructure, food security, and socio-economic systems. Although existing global climate models (GCMs) provide essential tools for climate prediction, they face limitations such as insufficient resolution and high computational costs when simulating extreme events. To address these issues, this study proposes a spatiotemporal downscaling model based on generative machine learning—the Domain Aligned Climate Downscaling model (DACD), designed to enhance the simulation capabilities for extreme weather events. The proposed model employs domain adaptation tricks and a Flow

Matching training framework to transform global low-resolution climate data into high-resolution local-scale climate information while achieving precise simulation of multivariable and temporal scales. The results show that during the historical period (2005–2014), our model outperformed existing methods in simulating high temperatures, extreme precipitation, strong wind, and tropical cyclone tracks, significantly reducing errors and improving the ability to capture extreme events. Under different future scenarios (2015–2100), the model reveals a significant increasing trend in the frequency and intensity of extreme events, particularly under the high-emission scenario (SSP585). Compared to traditional methods, our model more accurately simulates the spatial distribution and dynamic changes of extreme events, providing an essential tool for understanding the impacts of climate change. This study offers a new technological pathway for high-resolution climate analysis and extreme event prediction, providing scientific support for addressing future climate change and formulating adaptation strategies.

**Keywords:** Statistical Downscaling, Machine Learning, CMIP6, Extreme Events

## 1 Introduction

Climate change is amplifying extreme weather and climate events worldwide [1]. Decades of cumulative greenhouse gas emissions have influenced the balance of the climate system of the Earth, leading to more frequent and severe heat waves [2], cold spells[3], heavy precipitation[4], agricultural ecological droughts[5], and tropical cyclones (TC) such as typhoons and hurricanes [6]. These changes have already been observed. From 2016 to 2024, daily land temperature records show that extreme heat events occurred more than four times as often as statistically expected, while cold records dropped to half the anticipated frequency[7]. Such unprecedented changes bring cascading risks to human health, infrastructure, food security, and social economics. Therefore, dealing with future climate change, extreme weather, and climate events is necessary and urgent[8–10]. Climate mitigation and adaptation are highly dependent on accurate projections of future climate, and the Coupled Model Inter-comparison Project (CMIP) [11] serves as a valuable tool for predicting future climate states.

Since 1995, CMIP has been dedicated to organizing the comparison of coupled climate models, also known as general circulation models (GCM). CMIP5 introduced Representative Concentration Pathways (RCPs), while CMIP6 further integrated Shared Socioeconomic Pathways (SSPs) in ScenarioMIP, which can support consistent simulations of diverse socioeconomic and emissions trajectories through 2100, enabling a more integrated assessment of future climate risks.[12]. These advances have improved the scope and policy relevance of climate projections in assessing the potential impacts of climate change and transition strategies. However, there are inherent limitations in existing widely used GCMs, such as the European Consortium-Earth (EC-Earth)[13] and the Canadian Earth System Model (CanESM)[14]. These include

computationally expensive architectures with relatively coarse spatio-temporal resolutions (most are over 100 kilometers), as well as substantial systematic biases stemming from imperfect physical parameterization. Although the HighresMIP, another sub-project in CMIP6, provides higher-resolution simulations, it does not encompass the full spectrum of climate scenarios in the future and remains insufficient in capturing the magnitude and frequency of extreme events, particularly when compared with real-world observations and societal experiences[15].

What’s more, research shows that compared to the previous generation, CMIP6 has a limited improvement in the simulation of historical climate extremes. It tends to simulate a reduction in the warm bias in the mid-latitudes of South America and Asia[16]. In contrast, the cold bias in high latitudes still exists and has a relatively large amplitude. In addition, there is a wet bias in Tibet, northwest China, and the oceanic continent, while there is a dry bias in areas with frequent rainfall (southern China)[17]. In addition, due to spatio-temporal resolution limitation, most GCMs cannot accurately simulate extreme disasters such as TCs[18]. This will seriously affect GCM’s prediction of extreme events in future scenarios, hindering our comprehensive understanding of the coming climate transition path and climate action planning.

Since extreme events often occur on a local scale and require representation through medium to small-scale grids, many recent studies have employed downscaling methods to enhance the resolution of GCMs and improve the prediction of extreme events. The purpose of downscaling is to transform the outputs of large-scale climate models into high-resolution local data, which can be achieved primarily through two approaches: dynamic downscaling and statistical downscaling[19].

Dynamical downscaling employs high-resolution climate models, commonly known as regional climate models (RCMs), which are nested within GCMs to simulate regional climate processes at a finer spatial resolution, providing more detailed and accurate regional climate information[20]. Although GCMs have systematic biases, the inter-model spread is relatively large. As a result, most studies adopt a multi-model ensemble approach, using several GCMs to force advanced RCMs, such as the Weather Research and Forecasting (WRF) model, to generate various downscaling results[21]. This ensemble approach enables a more accurate analysis of extreme weather phenomena in the study area compared to using a single model. In addition, some studies focus on the impact of model configuration on the simulation of extreme events. Wehner et al. found that improving precipitation simulation quality can be achieved by using finer convection-permitting scale models [22]. Roberts et al. evaluated high-resolution models and demonstrated that a resolution of  $0.25^\circ$  provides the best performance for tropical cyclone simulations [18]. El-Samra et al. showed that downscaling techniques offer significant advantages for simulating extreme events in regions with complex terrain [23]. However, RCMs focus only on regional climate processes. Although they offer higher resolution, this comes at the cost of a reduced scope of analysis, limiting their application to local rather than global scales.

In contrast, statistical downscaling establishes statistical relationships between historical observations and GCM outputs, which are subsequently used to generate future climate projections[24]. The traditional quantile mapping (QM) [25] or Delta methods [26] are still popular. However, these methods assume a linear evolution of

bias patterns and fail to capture nonlinear climate changes, leading to a narrower spread between the methods. They still rely on large model ensembles, which exhibit significant inter-model spread, to reduce the extreme simulation error of a single model[27, 28].

With advances in reanalysis data[29] and improvements in computer hardware, deep learning-based statistical downscaling methods have been the state-of-the-art (SOTA) approach[30]. Vandal et al. first proposed Deep Statistical Downscaling (DeepSD) from the perspective of super-resolution[31]. A stacked deterministic Super-Resolution Convolutional Neural Network (SRCNN) outperforms traditional methods such as Bias Correction and Spatial Disaggregation (BCSD). He also noted that BCSD tends to overestimate the upper quantiles of precipitation, whereas DeepSD demonstrates greater stability. It is worth noting that during the training phase, the input for DeepSD is coarsely derived from labels, whereas during the inference phase it is directly inferred from the GCM outputs. This approach fails to account for the gap between training and inference inputs. Bano et al. highlighted that deterministic methods often underestimate extreme temperature and precipitation values because the variance of their predictions is significantly smaller than that of the observations.[32]. Therefore, they proposed Deep Ensemble Statistical Downscaling (DeepESD), which first reduces the systematic errors between multiple GCMs and observations through bias correction, and then generates downscaling results using a multi-model ensemble approach. Hess et al. introduced a probability-based model called the Consistency Model (CM), a post-distillation model built on the SDE training paradigm, which incorporates background field perturbations to achieve ensemble capabilities[33]. On the other hand, they degrade small-scale information by adding noise to ensure consistency between training and inference conditions. In the simulation of global average daily precipitation, the condition-aligned CM demonstrates a significant correction effect on the distribution of extreme precipitation events.

The above suggests that deep learning-based downscaling is gradually transitioning from deterministic multi-model approaches to probabilistic modeling with zero-shot capabilities. During this process, aligning training and inference inputs, known as domain alignment (DA), plays a crucial role. However, current research has yet to specifically analyze the impact of domain alignment on extreme event simulations. Furthermore, most studies focus on the spatial downscaling of single variables, such as temperature and precipitation, while the simulation of compound disasters, like TCs, also depends heavily on the multi-variables (like wind speed, mean sea level pressure and geopotential) and temporal scale. The TC tracks can be identified more accurately 6 hourly than on daily (in supplementary materials).

To address these issues, this study introduces a generative spatio-temporal downscaling model with domain alignment, Condition Alignment Climate Downscaling (CACD), built on the Flow Matching training paradigm, focusing on the simulation of extreme events in different climate scenarios in the future. Specifically, the transformation from the global daily / $0.70^\circ$  to 6 hours/ $0.25^\circ$  was achieved, involving seven ground variables. It also revealed the spatio-temporal frequency changes of extreme temperatures, extreme precipitation, strong winds, and tropical cyclones under various SSP scenarios.

## 2 Results

In this section, we present the results from two perspectives. First, during the historical period (2005–2014), we conduct a detailed comparison of the absolute error performance of each model and ERA5 at the 99th percentile. Second, under different future scenarios (2015–2100), we analyze the spatio-temporal variations in the area fraction and regional average frequency of future extreme events, including high temperatures, extreme precipitation, and strong wind events, which are respectively defined based on 2m temperature (T2M), 6-hourly total precipitation (TP), and 10m wind speed (WS10M). Additionally, we examine the spatio-temporal variations in the distribution and intensity of tropical cyclone (TC) tracks. In this study, European Consortium-Earth (EC-Earth) is used as the baseline model. The term "wo\_Domain\_Adaption" refers to the configuration without domain adaptation, while "Ours" represents the method proposed in this paper, DACD.

### 2.1 Evaluation in historical periods

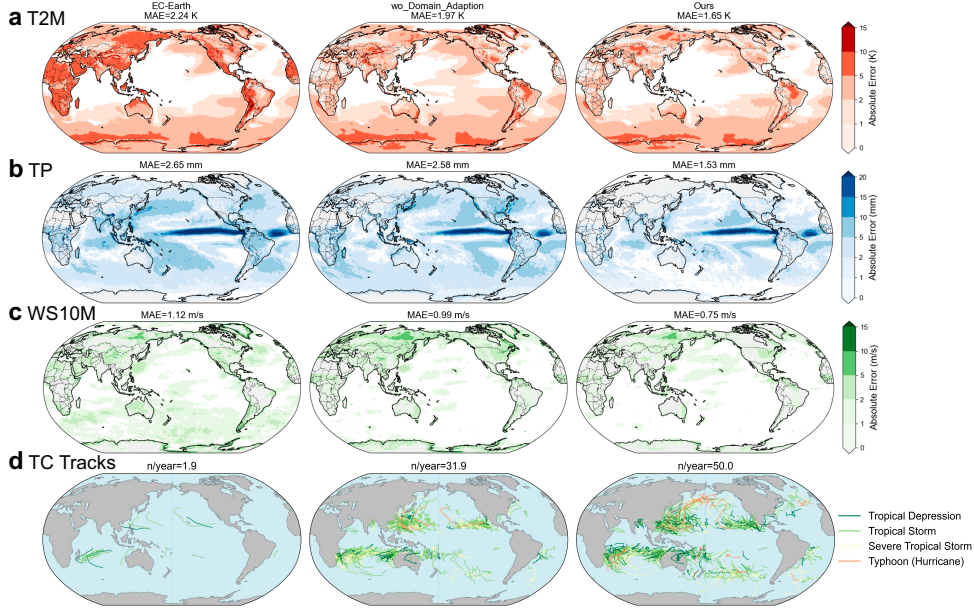


**Fig. 1 The evaluation results of the downscaling model from 2005 to 2014.** a to d correspond to T2M, TP, WS10M, and TC tracks, respectively. From left to right, the columns represent EC-Earth, wo\_Domain\_Adaption, and Ours, respectively. Specifically, panels a-c illustrate the spatial distribution of the 99th percentile MAE for each model, while panel d summarizes the number of tropical cyclones detected over the 10-year period along with their intensity classifications.

The results in Figure 1 indicate that Ours outperforms the other methods in capturing extreme values and reducing errors, particularly demonstrating significant advantages in TC detection and the simulation of extreme meteorological events.

Firstly, in the simulation of high temperatures, the MAE of Ours is 1.65K, significantly lower than the 2.24K of the EC-Earth model and 1.97K of wo\_Domain\_Adaption. From the perspective of spatial error distribution, Ours demonstrates outstanding performance in regions prone to high-temperature extreme events, such as tropical and subtropical areas, particularly across the African continent, northern South America, and Southeast Asia. The errors in these regions are markedly lower compared to the other two models. In contrast, EC-Earth exhibits substantial biases in these areas, especially within continental regions and near the equator, showing trends of overestimation or underestimation in extreme value. (Refer to supplementary materials for the bias distribution.) Although wo\_Domain\_Adaption shows some improvement, it still struggles to effectively capture extreme high-temperature events in these regions. Ours, however, achieves a more accurate simulation of extreme temperature distributions in these areas.

In the simulation of extreme precipitation, the MAE of the proposed model is 1.53 mm, significantly lower than the 2.65 mm of the EC-Earth model and 2.58 mm of wo\_Domain\_Adaption. From a spatial distribution perspective, the proposed model outperforms the other two models globally, particularly in simulating local precipitation in regions with strong monsoon activity (such as the South Asian monsoon region) and tropical areas, where it demonstrates greater accuracy. However, in the intertropical convergence zone (ITCZ), all three models exhibit certain deviations in their overall performance. Notably, the EC-Earth model and wo\_Domain\_Adaption show more pronounced precipitation biases in the ITCZ region, especially near the central Pacific Ocean and the Atlantic Ocean, where precipitation is systematically overestimated. (Refer to supplementary materials for the bias distribution.) Ours can better captures the dynamic characteristics of local precipitation changes.

In the simulation of strong winds, the MAE of Ours is 0.75 m/s, outperforming the 1.12 m/s of the EC-Earth model and 0.99 m/s of the baseline model. From the perspective of spatial error distribution, Ours demonstrates exceptional performance in coastal and marine regions, particularly in tropical cyclone-prone areas such as the Northwest Pacific, North Atlantic, and Indian Ocean. The wind speed simulation errors in these regions are significantly lower compared to the other two models. In contrast, the EC-Earth model often exhibits substantial deviations in these areas, especially near tropical cyclone paths, failing to accurately capture the spatial distribution characteristics of extreme wind speeds. (Refer to supplementary materials for the bias distribution.) Although wo\_Domain\_Adaption shows some improvement, it still presents deviations in land surface simulations. Ours, however, achieves more accurate simulations of wind speed variations in coastal and marine regions, particularly excelling in the precise simulation of strong wind events.

In the detection of TC tracks, Ours demonstrates significant advantages in the simulation of multivariable compound extreme weather events. While EC-Earth detected only approximately 2 per year and wo\_Domain\_Adaption detected 32, Ours successfully identified 50 cyclone paths per year, closely aligning with the actual observed

frequency of cyclone activity. The detection results based on ERA5 are provided in supplementary materials. Additionally, Ours effectively captures cyclone grades, including tropical depressions, tropical storms, severe tropical storms, and typhoons, comprehensively reflecting the intensity variations of cyclones. In contrast, EC-Earth’s performance in both the number of detected paths and intensity classification is unsatisfactory. Although wo\_Domain\_Adaption improves path detection, it still exhibits notable deviations in intensity classification, particularly in its weaker ability to detect strong typhoons. Ours excels in comprehensively simulating both the path distribution and intensity changes of cyclones.

In summary, Ours has demonstrated remarkable advantages in simulating extreme events during the historical period. Across the simulations of T2M, TP, WS10M, and TC Tracks, the model effectively reduces errors while accurately capturing the characteristics of extreme events. Notably, in TC tracks detection and intensity classification, Ours exhibits outstanding capabilities, underscoring its potential for high-resolution climate analysis and climate change impact assessment. Furthermore, the carbon emission trends and background conditions during the training period differ significantly from those of the testing period (detail in supplementary materials), further highlighting the model’s generalization ability under varying carbon emission scenarios. This model serves as a crucial tool for advancing the understanding of the mechanisms behind extreme weather events and for analyzing future trends under different carbon emission contexts.

## 2.2 The extreme on land in climate scenarios

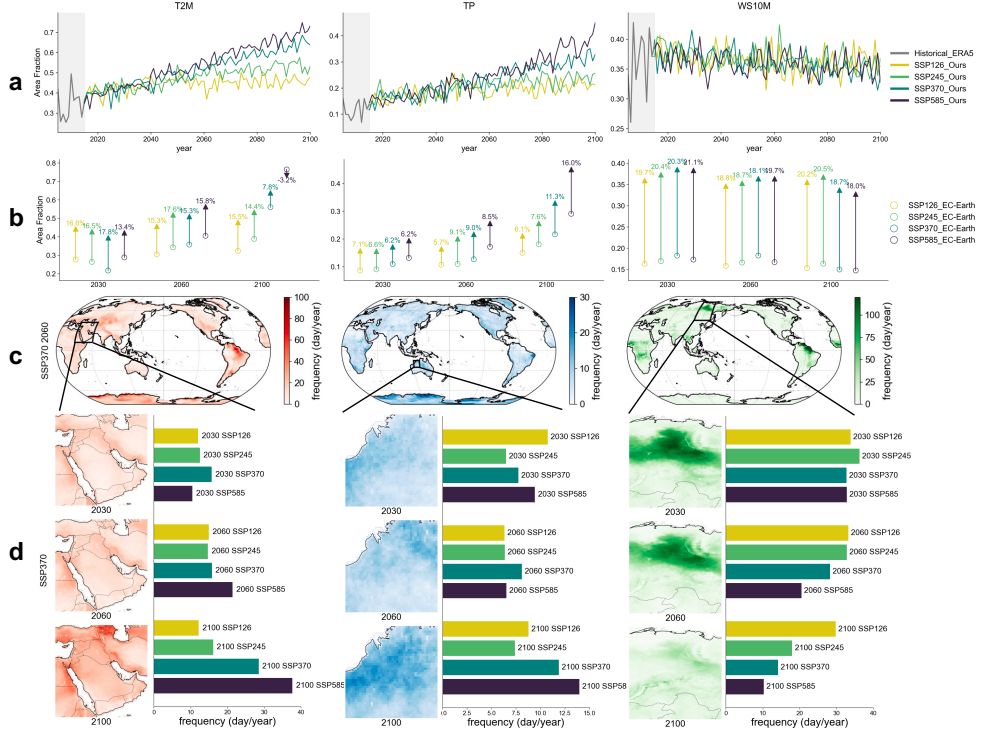


**Fig. 2** Spatiotemporal trends of high temperature (T2M), extreme precipitation (TP), and strong wind (WS10M) events over land under SSP scenarios (2015–2100): (a) Temporal trends of area fraction affected by the three types of extreme events; (b) The circles represent EC, while the arrows point to Ours. The length of the arrows indicates the magnitude of the correction, with longer arrows suggesting a larger difference between Ours and EC, and thus a greater correction. The correction values are annotated above the arrowheads, where positive values represent positive corrections, and negative values indicate negative corrections; (c) Global frequency distribution of extreme events in 2060 under the SSP370 scenario; (d) Spatial frequency distribution of extreme events in three climate-sensitive regions (Middle East, Northwestern Australia, and Siberia) under the SSP370 scenario, along with annual frequencies of extreme events for 2030, 2060, and 2100 under different scenarios.

The area fraction of high temperature and extreme precipitation events shown in Figure 2a exhibits a significant increasing trend under all SSP scenarios. Particularly under the high-emission scenario (SSP585), the area fraction of high temperature events demonstrates the most pronounced growth, indicating that the spatial coverage of extreme temperature events will expand significantly in the context of global warming. Similarly, the area fraction of extreme precipitation events also shows a notable increase, reflecting the profound impact of climate change on the global water cycle. In contrast, the area fraction of strong wind events shows a decreasing trend, with the rate of decline intensifying over time, especially under high-emission scenarios such as SSP585. This suggests that the spatial distribution of strong wind events may be suppressed by climate change, a trend that could be closely related to the weakening of the westerlies caused by global warming.

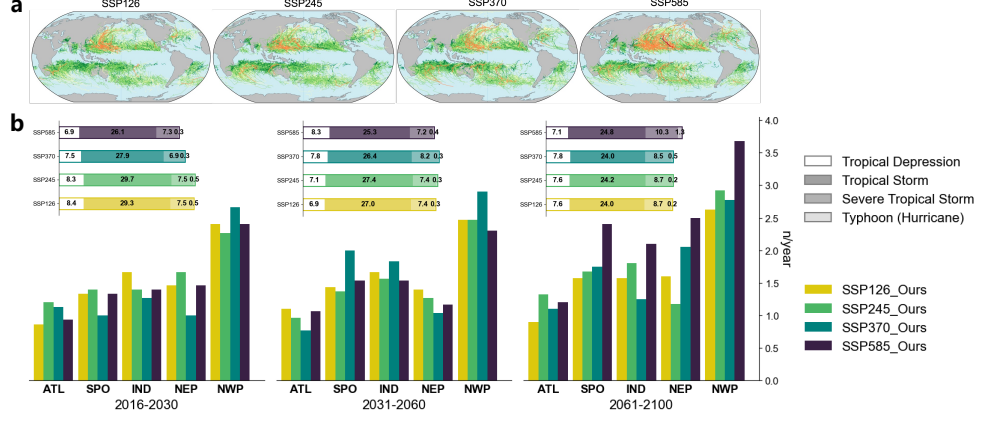


Figure 2b reveals that EC-Earth generally underestimates the area fraction of all types of extreme events in its simulations. This underestimation is evident across different scenarios, although the degree of discrepancy varies depending on the scenario. Over land, Ours detects up to 17.8% more high-temperature events (2030, SSP370), 16.0% more extreme precipitation events (2100, SSP585), and 20.5% more extreme strong wind events (2100, SSP245) compared to EC-Earth. Notably, for strong wind events, the incremental differences achieved by Ours consistently exceed 18% across all time periods and scenarios, demonstrating stable improvements in detection.

The frequency of extreme events exhibits significant spatial variations across different regions. Figure 2c shows the spatial distribution of global extreme event frequencies in 2060 under the SSP370 scenario, which represents the pathway most closely aligned with the current state of global socio-economic and environmental trends. High temperature events are primarily concentrated in East Asia, northeastern South America, and Antarctica. Extreme precipitation events are mainly distributed in Antarctica, eastern South America, and Australia. Strong wind events are predominantly concentrated in central Africa, Siberia, and northern South America.

The spatial distribution maps on the Figure 2d left reveal significant spatiotemporal changes in the frequency of extreme events within these regions during SSP370 2030–2100. The Middle East demonstrates a particularly notable increase in the frequency of extreme temperature events, indicating heightened sensitivity to temperature changes. In contrast, the spatial variations in extreme precipitation events in northwestern Australia are more complex, with certain areas experiencing rapid frequency increases while others show slower changes. Siberia displays a downward trend in the spatial frequency distribution of strong wind events, with both the coverage and frequency of occurrence decreasing significantly over time, especially under high-emission scenarios, where this decline is more pronounced. The bar charts on the Figure 2d right indicate that high temperature and extreme precipitation events occur significantly more frequently under high-emission scenarios (e.g., SSP585) compared to low-emission scenarios (e.g., SSP126), whereas the frequency of strong wind events shows a decreasing trend across all scenarios.

### 2.3 Detectable Tropical Cyclones under SSP scenarios



**Fig. 3** Detectable Tropical Cyclones under SSP Scenarios. (a) The cumulative spatial distribution of TC tracks under four SSP scenarios (SSP126, SSP245, SSP370, SSP585) from 2015 to 2100. (b) The upper stacked graph shows the incremental annual mean number of TC tracks detectable based on the output variables of Ours compared to EC-Earth under the four SSP scenarios. The color gradient corresponds to different TC grades. The lower bar chart summarizes the annual mean number of Severe Tropical Storms and Typhoons (or hurricanes) simulated in different ocean basins during three periods (2016–2030, 2031–2060, 2061–2100). Additionally, frequency statistics for Severe Tropical Storms and Typhoons (or hurricanes) are provided for regions with frequent TC activity. The ocean basins are abbreviated as follows: ATL (Atlantic Ocean), SPO (South Pacific Ocean), IND (Indian Ocean), NEP (Northeast Pacific Ocean), and NWP (Northwest Pacific Ocean).

TCs are fundamentally driven by oceanic heat release and exhibit their destructive power through extreme precipitation and strong winds, closely associated with key extreme meteorological factors. Our model demonstrates higher precision in identifying extreme heat, precipitation, and strong winds, thereby showcasing a significant advantage in detecting tropical cyclones. Furthermore, we simulated the TC tracks under future climate scenarios (Fig. 3a).

Under different SSP scenarios, the tracks and intensity distribution exhibit notable regional differences. For instance, under SSP126 (low-emission scenario), the tracks distribution remains relatively stable, with minimal spatial variation compare to history. In contrast, under SSP585 (high-emission scenario), the cumulative tracks density and intensity increase significantly, particularly in the Northwest Pacific and Northeast Pacific regions.

Compared to EC-Earth, the output variables from Ours achieve higher predictions for tropical cyclone tracks of varying grades across all SSP scenarios (Fig. 3b, upper stacked graph), particularly for Severe Tropical Storms and Typhoons (or Hurricanes). Under different SSP scenarios during the periods of 2016–2030, 2031–2060, and 2061–2100, our model detects an additional 43.7, 41.9, and 41.4 tracks per year, respectively, compared to EC-Earth. For Tropical Storms, the incremental tracks detected by our model are 25 times those detected by EC-Earth. Moreover, for Typhoons (or Hurricanes), a type of tropical cyclone undetectable by EC-Earth (see supplementary materials), our model captures 0.5 tracks per year. These results indicate that our

model demonstrates competitive precision in downscaling key tropical cyclone-related variables, resulting in higher sensitivity in detecting tropical cyclone occurrences. This enhanced sensitivity allows our model to capture more impacts of climate change drivers on tropical cyclone activity.

For Severe Tropical Storms and Typhoons (or Hurricanes), which pose significant potential threats to socio-economic systems, the number of tropical cyclones exhibits a notable increasing trend across different regions over time and under intensified emission scenarios (Fig. 3b, lower bar chart). Particularly under the high-emission scenario (SSP585), the number of tropical cyclones in the Northeast Pacific (NEP) and Northwest Pacific (NWP) increases significantly, reaching 2.4 and 3.7 tracks per year, respectively, during 2061–2100 representing a 60% and 48% increase compared to 2016–2030. In contrast, changes in the Atlantic (ATL) and Indian Ocean (IND) are relatively minor. This regional disparity is closely related to the varying impacts of climate change on regional oceanic and atmospheric conditions. For instance, this change is likely associated with stronger sea surface temperature increases under the high-emission scenario (see supplementary materials), as warmer oceans provide more abundant energy for the formation and maintenance of tropical cyclones. This trend underscores the need for enhanced disaster prevention and mitigation efforts in coastal regions, especially under high-emission scenarios, as tropical cyclones could pose greater threats to ecosystems and socio-economic systems in these areas.

## 3 Method

### 3.1 Data

The ERA5 reanalysis dataset, produced by the European Centre for Medium-Range Weather Forecasts (ECMWF), provides hourly data starting from January 1940, with a spatial resolution of approximately 31 km [34]. Renowned for its extensive coverage and high accuracy, this dataset serves as the foundation for our study. In this study, we utilize ERA5 data resampled to a spatial resolution of  $0.25^\circ$  (corresponding to  $720 \times 1440$  grid points globally) and a temporal resolution of 6 hours, as targets. Additionally, a coarser daily-mean version with a spatial resolution of approximately 70 km (corresponding to  $256 \times 512$  grid points globally) is used as the guiding condition. The dataset is split into two subsets: the first spanning from 1940 to 2000, is used for model training, while the second subset, covering the period from 2005 to 2014, is reserved for testing. The ERA5 variables employed in this study include 2-meter temperature (T2M), 10-meter u wind component (U10M), 10-meter v wind component (V10M), mean sea level pressure (MSL), 6 hourly total precipitation (TP), and geopotential (Z) at 250 hPa (Z250) and 500 hPa (Z500). The selection of variables such as Z250 and Z500 is specifically aimed at detecting TC-related atmospheric features.

EC-Earth, a GCM participating in CMIP6, is developed collaboratively by several European meteorological and research institutions [13]. It is widely applied for climate projection and weather forecasting research. In this study, we select the standard EC-Earth configuration with daily outputs at 70 km resolution ( $256 \times 512$  grid points). The historical data from 1940 to 2000 is used for model training, while the

data from 2005 to 2014 is used for testing. Additionally, future projections from ScenarioMIP (2015-2100) under four future scenarios (SSP126, SSP245, SSP370, and SSP585) are used for inference and analysis of extreme weather events. The CMIP6 variables employed in this study include near-surface air temperature (TAS), eastward near-surface wind (UAS), northward near-surface wind (VAS), and sea level pressure (PSL), which correspond to ERA5 variables T2M, U10M, V10M, and MSL, respectively. Additional variables include precipitation rate (PR), and geopotential height (ZG). To ensure consistency, we reference all variables using ERA5 nomenclature throughout the paper.

We also incorporate topographic data from the Global Elevation and Continental-scale Ocean Bathymetry (GENCO), a high-resolution global digital elevation dataset that includes both terrestrial and seafloor topography, commonly utilized in topographic, oceanic, and environmental science research [35]. This dataset integrates land elevation and ocean bathymetry data, offering a unified reference framework for analyzing Earth’s surface characteristics. The original 30 m resolution GENCO data are resampled to 0.25° resolution for this study, while preserving elevation extrema.

Only month of year and day of year are used as temporal features, which are encoded into the model using sine and cosine transformations. A summary of all data sources, variables, abbreviations, and their respective roles is presented in the table below:

**Table 1** Overview of data sources, variables, abbreviations, and their roles in the study. The table includes variables from ERA5 (used as labels and conditions), EC-Earth (used as conditions), GENCO (used as elevation condition), and temporal information (month and day of year). Resolution details are also provided for each role.

Source	Full name	Abbreviation	Role
ERA5	2-meter temperature	T2M	label (6hourly/0.25°) & condition (daily/70km)
	10-meter u wind component	U10M	label (6hourly/0.25°) & condition (daily/70km)
	10-meter v wind component	V10M	label (6hourly/0.25°) & condition (daily/70km)
	mean sea-level pressure	MSL	label (6hourly/0.25°) & condition (daily/70km)
	total precipitation	TP	label (6hourly/0.25°) & condition (daily/70km)
	geopotential	Z	label (6hourly/0.25°) & condition (daily/70km)
EC-Earth	Near-Surface Air Temperature	TAS	condition (daily/70km)
	Eastward Near-Surface Wind	UAS	condition (daily/70km)
	Northward Near-Surface Wind	VAS	condition (daily/70km)
	Sea Level Pressure	PSL	condition (daily/70km)
	Precipitation Flux	PR	condition (daily/70km)
	Geopotential Height	ZG	condition (daily/70km)
GENCO	Digital Elevation Model	DEM	condition (0.25°)
Temporal	Month of year	Month	condition
	Day of year	Doy	condition

Except for digital elevation model (DEM) data, which is normalized using the min-max method, all other variables are processed using z-score normalization. Special preprocessing is applied to TP and Z during this process to address their distinct statistical characteristics.

To mitigate the challenges in model training caused by the long-tail distribution of TP, we first apply a logarithmic transformation,  $\log(x + 1)$ , followed by normalization of the transformed data. Additionally, the PR and ZG variables from EC-Earth are converted to align with ERA5 variables. Specifically, PR is multiplied by 86,400 (the number of seconds in a day) to obtain daily cumulative precipitation, while ZG is multiplied by the gravitational acceleration constant ( $9.81 \text{ m/s}^2$ ) to produce Z.

### 3.2 Non-Blind Statistical Downscaling with Domain Adaption

Due to the distinct origins of ERA5 and EC-Earth, the degradation kernel mapping from ERA5 to EC-Earth is unknown. In the context of computer vision, the term "degradation kernel" refers to a mathematical or computational function that models how high-resolution data (such as ERA5) is systematically transformed into lower-resolution data (such as EC-Earth). This transformation typically involves processes such as smoothing, introducing noise, or other unknown degradation mechanisms, which can alter the quality or resolution of the original data in ways that are not fully understood. As a result, experiments using EC-Earth as input and ERA5 as target data can be considered a blind super-resolution task. Under this setting, performance was not optimal (see supplementary materials). Inspired by previous studies [31–33] on , we reformulate the complex end-to-end blind super-resolution task into a pipeline consisting of non-blind super-resolution and domain adaptation. During the training process, the model learns to reconstruct high-resolution ERA5 fields ( $0.25^\circ/6\text{hourly}$ ) from degraded versions ( $70\text{km}/\text{daily}$ ) obtained by interpolation, while simultaneously aligning the hidden feature distributions of degraded ERA5 and EC-Earth. The ultimate goal is to map daily 70 km resolution EC-Earth inputs, such as T2M, U10M, V10M, MSL, TP, Z250, Z500, DEM, and temporal features, to a 6 hourly outputs at  $0.25^\circ$  resolution for T2M, U10M, V10M, MSL, TP, Z250, and Z500.

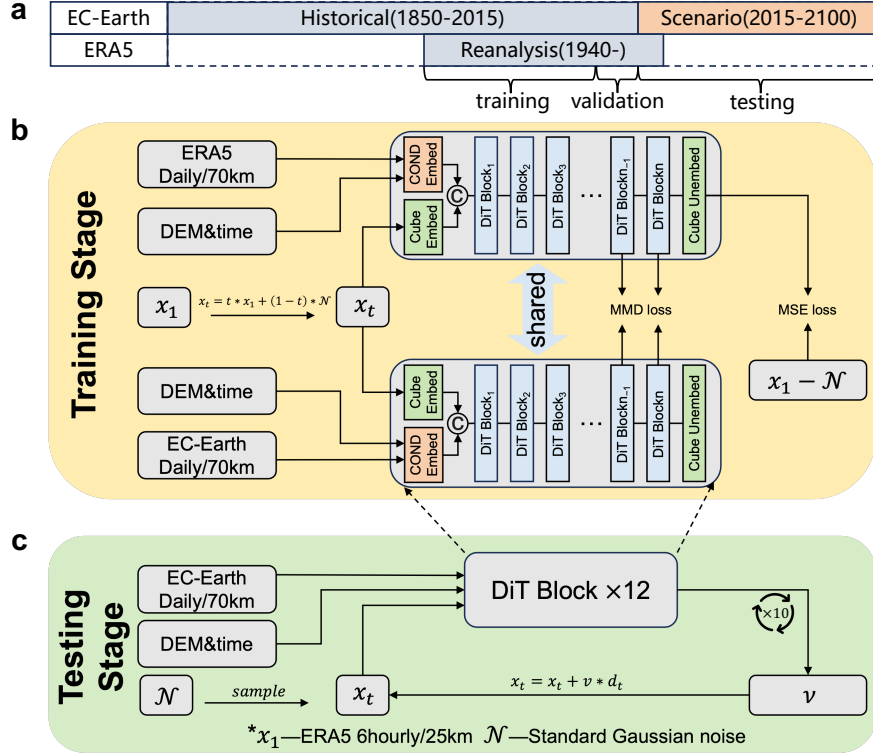


**Fig. 4** Overview of the model architecture. (a) Data sources and timeline, including EC-Earth (historical and scenario data) and ERA5 reanalysis data. The dataset is split into training, validation, and testing sets. (b) Training stage: The model learns to reconstruct ERA5 fields at 6-hourly,  $0.25^\circ$  resolution from degraded ERA5 inputs at daily, 70km resolution, while aligning feature distributions between degraded ERA5 and EC-Earth using Maximum Mean Discrepancy (MMD) loss. DEM and temporal features are included as additional conditions. (c) Testing stage: The trained model takes EC-Earth (daily, 70km resolution), along with DEM and temporal features, as inputs and generates downscaled outputs (ERA5 variables at 6-hourly,  $0.25^\circ$  resolution) through iterative refinement. Gaussian noise is utilized to initialize the sampling process.

The training stage primarily incorporates two key components: a Flow Matching-based generation framework [36] and a feature alignment strategy leveraging Maximum Mean Discrepancy (MMD) [37].

Flow Matching is a diffusion-based framework that learns a continuous velocity field between distributions, capturing the dynamic transformation process in a more efficient and precise manner. Unlike conventional diffusion models (e.g., DDPM), Flow Matching directly models the velocity of distribution changes, significantly reducing the number of sampling steps while enhancing the fidelity and stability of the generated outputs. This approach provides a novel perspective for optimizing diffusion-based generative models. In this study, we treat one day as the smallest sampling unit. The target distribution is high resolution ERA5 data (6-hourly,  $0.25^\circ$ ), and the conditional

input consists of low resolution data (daily, 70 km) from two domains: degraded ERA5 (source domain) and EC-Earth (target domain).

The Flow Matching backbone is built upon vanilla Diffusion Transformer (DiT), augmented with a condition embedding module, a cube embedding module at the head, a cube unembedding module at the tail, and the stacked 12-layer DiT Blocks in the middle. Specifically, the condition embedding module first interpolates the source domain conditions into shape (7, 720, 1440). Temporal information is encoded using sine and cosine, expanded across spatial dimensions to shape (4, 720, 1440), and concatenated with the DEM (1 channel), producing a 12-channel tensor (12, 720, 1440). A two-dimensional (2D) convolutional layer kernel size 3, stride 1, and padding 1 (denoted k3s1p1) transforms this into a condition feature map of shape (32, 720, 1440). In the cube embedding module, to avoid increasing the computational cost of three-dimensional (3D) convolutions, the noisy high spatiotemporal ERA5 data (4, 7, 720, 1440) is split along the temporal dimension into four slices. Each slice is processed independently by a 2D convolutional layer (k3s1p1), producing target features of (32, 720, 1440). Finally, these are concatenated with condition features and passed through another 2D convolutional layer (k3s1p1) to reduce the channels to 32. Standard Gaussian noise ( $\mathcal{N}$ ) is added according to

$$x_t = t \times x_1 + (1 - t) \times \mathcal{N}$$

where  $t \in [0, 1]$ ,  $x_1$  represents the 6-hourly/0.25° ERA5 data, and  $x_t$  represents the ERA5 data with added noise.

Before entering the DiT blocks, features undergo patch embedding (patch size = 16, hidden dimension = 768). The backbone consists of 12 stacked DiT blocks, each with 6 attention heads. Additionally, the noisy step is encoded using sine and cosine functions, and repeated to match the feature dimensions, and added element-wise to the features. After being processed by the DiT blocks, features are ultimately restored to the 2D spatial domain through patch unembedding, and followed by cube unembedding. The design of the cube unembedding module mirrors that of the cube embedding module: four independent 2D convolutional layers (k3s1p1) reconstructs outputs for the four temporal slices. The final output, velocity  $v$ , is compared with the target  $x_1 - \mathcal{N}$  using mean squared error (MSE):

$$\mathcal{L}_{\text{MSE}} = \|v - (x_1 - \mathcal{N})\|^2$$

For EC-Earth inputs, the same model structure and processing steps are applied. This ensures that two distinct hidden feature sets are extracted from the last three layers of the DiT blocks, each conditioned separately on the source and target domains. These two feature sets are then mapped to a common Hilbert space, where the MMD is computed and incorporated into the optimization objective. The MMD loss is defined as:

$$\mathcal{L}_{\text{MMD}} = \frac{1}{n^2} \sum_{i=1}^n \sum_{j=1}^n k(x_i, x_j) + \frac{1}{m^2} \sum_{i=1}^m \sum_{j=1}^m k(y_i, y_j) - \frac{2}{nm} \sum_{i=1}^n \sum_{j=1}^m k(x_i, y_j) \quad (1)$$

where  $X = \{x_1, x_2, \dots, x_n\}$  and  $Y = \{y_1, y_2, \dots, y_m\}$  represent the source and target domain features sets, respectively. Here,  $n$  and  $m$  denote the sample sizes for the source and target domains, and  $k(x, y)$  is the kernel function. A Gaussian kernel ( $k$ ) is adopted, with bandwidth  $\sigma$ :

$$k(x, y) = \exp\left(-\frac{\|x - y\|^2}{2\sigma^2}\right) \quad (2)$$

Thus, the overall loss function combines the MSE and the MMD terms:

$$L = L_{\text{MSE}} + L_{\text{MMD}} \quad (3)$$

During the testing stage, the model takes as input the initial noise field, EC-Earth, DEM, and temporal features. The high-resolution noise initial  $x_t$  for iterative denoising is sampled from a standard Gaussian distribution. The iterative denoising process is governed by the following formula:

$$x'_t = x_t + v \times d_t \quad (4)$$

where  $x_t$  represents the downsampled field before the update,  $x'_t$  represents the downsampled field after the update,  $v$  denotes the velocity field predicted by the model, and  $d_t$  represents the time differential. Note that  $d_t$  is defined as the reciprocal of the denoising step count.

The model was trained and tested on two NVIDIA Tesla A100 GPUs. Training employed the AdamW optimizer with an initial learning rate of  $1 \times 10^{-4}$ , decayed by 10% every 50 epochs using a StepLR scheduler, over a total of 200 epochs. During testing, the number of denoising steps was set to 10.

### 3.3 Extreme detection

High temperature, extreme precipitation, and strong wind events were identified using percentile-based methods. First, calculate the 99th percentile of ERA5 data for the reference period 1979-2000. For each grid point, values exceeding this threshold are assigned a value of 1, and all others are assigned 0. Summing up all grid points for a given time sample yields the total frequency of extreme events at that timestamp. Dividing by the total number of grid points provides the area fraction of the spatial domain affected by extreme events.

TC tracks were detected using the TempestExtremes [38], a versatile toolkit developed by the Climate and Global Change Research Team at the University of California, Davis. TempestExtremes is designed for identifying and tracking extreme weather events in large-scale climate datasets. We applied it to detect the number of tropical cyclones in ERA5 daily and 6-hourly datasets, and found significant differences between the results. Please refer to the supplementary materials for details. Parameters settings for the detection and suture operators are detailed in supplementary



materials. The intensity of tropical cyclones is defined according to the national standard [39], which classifies grades based on the maximum WS10M along one TC track. The grades discussed in this article are as follows:

**Table 2** Tropical cyclone grades based on national standard [39]

Maximum WS10M (m/s)	Grade
10.8–17.1	Tropical Depression
17.2–24.4	Tropical Storm
24.5–32.6	Severe Tropical Storm
32.7–41.4	Typhoon (Hurricane)
41.5–50.9	Severe Typhoon (Hurricane)

### 3.4 Evaluation method

The evaluation framework includes two main components: 1) calculation of two distinct sets of spatial quantile distributions from ERA5 for different purposes; and 2) assessment of model performance in the historical scenario (2005–2014), using mean absolute error (MAE) of quantiles, with statistical significance determined via bootstrap resampling.

Two sets of ERA5 spatial quantile distributions are calculated. The first set is derived from the 1st, 5th, 10th, 90th, 95th, and 99th percentiles over 2005–2014, used as the reference (“ground truth”). For each model, the MAE between these reference quantiles and the corresponding quantiles obtained from the downscaling outputs quantifies the ability to reproduce extreme climate states during the validation period. The MAE for a given quantile  $q$  is computed as:

$$\text{MAE}_q = \frac{1}{n_x n_y} \sum_{i=1}^{n_x} \sum_{j=1}^{n_y} \left| P_{\text{model},i,j}^q - P_{\text{ERA5},i,j}^q \right| \quad (5)$$

where  $n_x$  and  $n_y$  represent the number of grid points in the longitude and latitude directions respectively.  $i$  and  $j$  are the indices for longitude and latitude directions respectively.  $P_{\text{model},i,j}^q$  and  $P_{\text{ERA5},i,j}^q$  represent the values at the  $i, j$  grid point for the model and ERA5 quantile data respectively.

The second set uses the 99th percentile over 1979–2000 as a historical benchmark to identify extreme pixels. This enables analysis of spatiotemporal changes in future extreme events. Extreme event frequency is obtained counting the number of occurrences, while the area fraction is calculated as the ratio of extreme pixels to the total number of spatial pixels.

For significance testing, model downscaling results for 2005–2014 are grouped into four timestamps (00, 06, 12, and 18 UTC), with each group containing approximately 3,600 samples. From each group, 300 samples are randomly drawn with replacement, and the 99th percentile is recalculated. The MAE (Equation 5) relative to the corresponding ERA5 quantile is then determined.

## 4 Discussion

This study proposes a generative machine learning-based downscaling model aimed at addressing the issues of insufficient resolution and extreme value biases in existing climate models when simulating extreme weather events. Through model evaluation during the historical period (2005–2014) and simulations of extreme events under different future scenarios (2015–2100), the results demonstrate that Ours exhibits significant advantages in accurately capturing the spatiotemporal characteristics of extreme weather events.

Firstly, during the historical period, Ours significantly reduces errors in the simulation of high temperatures, extreme precipitation, and strong wind. This is particularly evident in the simulation of high-temperature events in tropical and subtropical regions, localized precipitation in monsoon heavy rainfall areas, and wind speeds in regions frequently affected by tropical cyclones. Compared to the other model and the EC-Earth, Ours demonstrates higher accuracy and stability. These results indicate that the combination of domain adaptation strategies and a generative downscaling framework effectively mitigates the shortcomings of existing climate models in terms of spatial resolution and extreme values biases, while enhancing the ability to simulate extreme events. Furthermore, the model’s robustness to varying carbon emission backgrounds is evidenced by its improved accuracy on test datasets, where emission contexts differ significantly from the training set, further supporting its applicability to future scenario predictions. In addition, Ours excels in detecting tropical cyclone tracks and classifying their intensity, fully capturing the intensity variations and spatial distribution of cyclones. This capability is of great importance for understanding the mechanisms behind extreme weather events and their potential impacts.

In the simulations under different climate scenarios, the study reveals that the area fraction of high temperature and extreme precipitation events shows a significant increasing trend across all SSP scenarios, especially under the high-emission scenario (SSP585), where the growth in the area fraction of high temperature events is most pronounced. This indicates that with the increase in greenhouse gas emissions, the frequency and intensity of extreme weather events will further intensify, posing significant threats to global ecosystems and socio-economic systems. Furthermore, using the proposed model, the spatial frequency variations of extreme events were analyzed in climate-sensitive regions such as the Middle East, northwestern Australia, and Siberia. Interestingly, it was found that the frequency of strong wind events is expected to decrease counterintuitively.

Although Ours demonstrates significant advantages in simulating extreme events, certain limitations remain. Firstly, there are still some biases in the precipitation simulations for the ITCZ, which may be related to the complex climate dynamics and inconsistencies in data sources. Additionally, while the domain adaptation strategy effectively reduces biases between different data sources, further optimization of the model’s multivariable coupling capabilities is necessary to improve the predictive performance for compound extreme events.

Future research can further explore the following aspects: First, optimizing the model’s training strategies, particularly for multivariable coupled simulations in complex regions, to improve the predictive capability for compound extreme events;

second, expanding the application scope of the model to simulate other climate variables, such as ocean dynamics and polar climate changes; third, incorporating more observational data and high-resolution reanalysis data to further enhance the model's accuracy and applicability. Moreover, with the continuous advancement of generative machine learning technologies, future studies can explore more advanced generative model frameworks to further improve the efficiency and precision of downscaling simulations.

In summary, the proposed downscaling model provides an important tool for high-resolution climate analysis and climate change impact assessments. It effectively captures the spatiotemporal trends of extreme weather events and offers reliable predictions for climate change trends under different carbon emission scenarios. This study not only provides a new technical pathway for climate science but also offers critical scientific support for addressing future climate changes and formulating adaptation strategies.

## Data Availability Statement

The EC-Earth data are accessible through the Earth System Grid Federation at <https://esgf-ui.ceda.ac.uk/cog/search/cmip6-ceda/>. The ERA5 reanalysis data are accessible through the Copernicus Climate Data Store at <https://cds.climate.copernicus.eu/>.

## Code Availability Statement

The TempestExtremes tracker used in this study is available from <https://github.com/ClimateGlobalChange/tempestextremes>.

## Acknowledgements

We gratefully acknowledge the ECMWF for their efforts in producing, maintaining, and distributing the ERA5 reanalysis data. We thank the European consortium of national meteorological services and research institutes for developing and distributing EC-Earth data.

## Competing interests

The authors declare no competing interests.

## References

- [1] Tripathy, K.P., Mukherjee, S., Mishra, A.K., Mann, M.E., Williams, A.P.: Climate change will accelerate the high-end risk of compound drought and heatwave events. *Proceedings of the National Academy of Sciences* **120**(28), 2219825120 (2023)

- [2] Raymond, C., Matthews, T., Horton, R.: The emergence of heat and humidity too severe for human tolerance, *Sci. Adv.*, 6, eaaw1838 (2020)
- [3] Ruosteenoja, K., Jylhä, K.: Extreme cold days and spells in northern europe at 0.5 c–2.0 c global warming levels. *International Journal of Climatology*, 8875 (2025)
- [4] Fowler, H.J., Blenkinsop, S., Green, A., Davies, P.A.: Precipitation extremes in 2023. *Nature Reviews Earth & Environment* **5**(4), 250–252 (2024)
- [5] Pizzorni, M., Innocenti, A., Tollin, N.: Droughts and floods in a changing climate and implications for multi-hazard urban planning: A review. *City and Environment Interactions*, 100169 (2024)
- [6] Calvin, K., Dasgupta, D., Krinner, G., Mukherji, A., Thorne, P.W., Trisos, C., Romero, J., Aldunce, P., Barret, K., Blanco, G., et al.: *Ipcc, 2023: Climate change 2023: Synthesis report, summary for policymakers. contribution of working groups i, ii and iii to the sixth assessment report of the intergovernmental panel on climate change [core writing team, h. lee and j. romero (eds.)]. ipcc, geneva, switzerland. IPCC, 2023: Climate Change 2023: Synthesis Report. Contribution of Working Groups I, II and III to the Sixth Assessment Report of the Intergovernmental Panel on Climate Change [Core Writing Team, H. Lee and J. Romero (eds.)]. IPCC, Geneva, Switzerland., 1–34 (2023)*
- [7] Fischer, E.M., Bador, M., Huser, R., Kendon, E.J., Robinson, A., Sippel, S.: Record-breaking extremes in a warming climate. *Nature Reviews Earth & Environment*, 1–15 (2025)
- [8] Newman, R., Noy, I.: The global costs of extreme weather that are attributable to climate change. *Nature Communications* **14**(1), 6103 (2023)
- [9] El Garroussi, S., Di Giuseppe, F., Barnard, C., Wetterhall, F.: Europe faces up to tenfold increase in extreme fires in a warming climate. *npj Climate and Atmospheric Science* **7**(1), 30 (2024)
- [10] Xu, L., Lin, N., Poor, H.V., Xi, D., Perera, A.: Quantifying cascading power outages during climate extremes considering renewable energy integration. *Nature communications* **16**(1), 2582 (2025)
- [11] Meehl, G.A., Boer, G.J., Covey, C., Latif, M., Stouffer, R.J.: The coupled model intercomparison project (cmip). *Bulletin of the American Meteorological Society* **81**(2), 313–318 (2000)
- [12] O'Neill, B.C., Tebaldi, C., Van Vuuren, D.P., Eyring, V., Friedlingstein, P., Hurtt, G., Knutti, R., Kriegler, E., Lamarque, J.-F., Lowe, J., et al.: The scenario model intercomparison project (scenariomip) for cmip6. *Geoscientific Model Development* **9**(9), 3461–3482 (2016)

- [13] Döscher, R., Acosta, M., Alessandri, A., Anthoni, P., Arneth, A., Arsouze, T., Bergmann, T., Bernadello, R., Bousetta, S., Caron, L.-P., *et al.*: The ec-earth3 earth system model for the climate model intercomparison project 6. Geoscientific Model Development Discussions **2021**, 1–90 (2021)
- [14] Swart, N.C., Cole, J.N., Kharin, V.V., Lazare, M., Scinocca, J.F., Gillett, N.P., Anstey, J., Arora, V., Christian, J.R., Hanna, S., *et al.*: The canadian earth system model version 5 (canesm5. 0.3). Geoscientific Model Development **12**(11), 4823–4873 (2019)
- [15] Haarsma, R.J., Roberts, M.J., Vidale, P.L., Senior, C.A., Bellucci, A., Bao, Q., Chang, P., Corti, S., Fučkar, N.S., Guemas, V., *et al.*: High resolution model intercomparison project (highresmip v1. 0) for cmip6. Geoscientific Model Development **9**(11), 4185–4208 (2016)
- [16] Kim, Y.-H., Min, S.-K., Zhang, X., Sillmann, J., Sandstad, M.: Evaluation of the cmip6 multi-model ensemble for climate extreme indices. Weather and Climate Extremes **29**, 100269 (2020)
- [17] Dong, T., Dong, W.: Evaluation of extreme precipitation over asia in cmip6 models. Climate Dynamics **57**(7), 1751–1769 (2021)
- [18] Roberts, M.J., Camp, J., Seddon, J., Vidale, P.L., Hodges, K., Vannière, B., Mecking, J., Haarsma, R., Bellucci, A., Scoccimarro, E., *et al.*: Projected future changes in tropical cyclones using the cmip6 highresmip multimodel ensemble. Geophysical research letters **47**(14), 2020–088662 (2020)
- [19] Hewitson, B.C., Crane, R.G.: Climate downscaling: techniques and application. Climate Research **7**(2), 85–95 (1996)
- [20] Xu, Z., Han, Y., Yang, Z.: Dynamical downscaling of regional climate: A review of methods and limitations. Science China Earth Sciences **62**, 365–375 (2019)
- [21] Zobel, Z., Wang, J., Wuebbles, D.J., Kotamarthi, V.R.: High-resolution dynamical downscaling ensemble projections of future extreme temperature distributions for the united states. Earth’s Future **5**(12), 1234–1251 (2017)
- [22] Wehner, M.F., Reed, K.A., Li, F., Prabhat, Bacmeister, J., Chen, C.-T., Paciorek, C., Gleckler, P.J., Sperber, K.R., Collins, W.D., *et al.*: The effect of horizontal resolution on simulation quality in the community atmospheric model, cam 5.1. Journal of Advances in Modeling Earth Systems **6**(4), 980–997 (2014)
- [23] El-Samra, R., Bou-Zeid, E., Bangalath, H.K., Stenchikov, G., El-Fadel, M.: Seasonal and regional patterns of future temperature extremes: high-resolution dynamic downscaling over a complex terrain. Journal of Geophysical Research: Atmospheres **123**(13), 6669–6689 (2018)

- [24] Wilby, R.L., Dawson, C.W.: The statistical downscaling model: insights from one decade of application. *International Journal of Climatology* **33**(7) (2013)
- [25] Maraun, D.: Bias correction, quantile mapping, and downscaling: Revisiting the inflation issue. *Journal of Climate* **26**(6), 2137–2143 (2013)
- [26] Hay, L.E., Wilby, R.L., Leavesley, G.H.: A comparison of delta change and down-scaled gcm scenarios for three mountainous basins in the united states 1. *JAWRA Journal of the American Water Resources Association* **36**(2), 387–397 (2000)
- [27] Tefera, G.W., Ray, R.L., Wootten, A.M.: Evaluation of statistical downscaling techniques and projection of climate extremes in central texas, usa. *Weather and Climate Extremes* **43**, 100637 (2024)
- [28] Miller, S., Ormaza-Zulueta, N., Koppa, N., Dancer, A.: Statistical downscaling differences strongly alter projected climate damages. *Communications Earth & Environment* **6**(1), 145 (2025)
- [29] Hersbach, H., Bell, B., Berrisford, P., Biavati, G., Horányi, A., Muñoz Sabater, J., Nicolas, J., Peubey, C., Radu, R., Rozum, I., et al.: ERA5 hourly data on single levels from 1940 to present, Copernicus Climate Change Service (C3S) Climate Data Store (CDS)[data set] (2023)
- [30] Sun, Y., Deng, K., Ren, K., Liu, J., Deng, C., Jin, Y.: Deep learning in statistical downscaling for deriving high spatial resolution gridded meteorological data: A systematic review. *ISPRS Journal of Photogrammetry and Remote Sensing* **208**, 14–38 (2024)
- [31] Vandal, T., Kodra, E., Ganguly, S., Michaelis, A., Nemani, R., Ganguly, A.R.: DeepSD: Generating high resolution climate change projections through single image super-resolution. In: *Proceedings of the 23rd Acm Sigkdd International Conference on Knowledge Discovery and Data Mining*, pp. 1663–1672 (2017)
- [32] Baño-Medina, J., Manzananas, R., Cimadevilla, E., Fernández, J., González-Abad, J., Cofiño, A.S., Gutiérrez, J.M.: Downscaling multi-model climate projection ensembles with deep learning (deepesd): contribution to cordex eur-44. *Geoscientific Model Development Discussions* **2022**, 1–14 (2022)
- [33] Hess, P., Aich, M., Pan, B., Boers, N.: Fast, scale-adaptive and uncertainty-aware downscaling of earth system model fields with generative machine learning. *Nature Machine Intelligence*, 1–11 (2025)
- [34] Soci, C., Hersbach, H., Simmons, A., Poli, P., Bell, B., Berrisford, P., Horányi, A., Muñoz-Sabater, J., Nicolas, J., Radu, R., et al.: The era5 global reanalysis from 1940 to 2022. *Quarterly Journal of the Royal Meteorological Society* **150**(764), 4014–4048 (2024)

- [35] Mayer, L., Jakobsson, M., Allen, G., Dorschel, B., Falconer, R., Ferrini, V., Lamarche, G., Snaith, H., Weatherall, P.: The nippon foundation—gebco seabed 2030 project: The quest to see the world’s oceans completely mapped by 2030. *Geosciences* **8**(2), 63 (2018)
- [36] Lipman, Y., Chen, R.T., Ben-Hamu, H., Nickel, M., Le, M.: Flow matching for generative modeling. *arXiv preprint arXiv:2210.02747* (2022)
- [37] Gretton, A., Borgwardt, K., Rasch, M., Schölkopf, B., Smola, A.: A kernel method for the two-sample-problem. *Advances in neural information processing systems* **19** (2006)
- [38] Ullrich, P.A., Zarzycki, C.M., McClenny, E.E., Pinheiro, M.C., Stansfield, A.M., Reed, K.A.: Tempestextremes v2. 1: A community framework for feature detection, tracking, and analysis in large datasets. *Geoscientific Model Development* **14**(8), 5023–5048 (2021)
- [39] Quality Supervision, I., China, Q., China, S.A.: Grade of Tropical Cyclones. First published in 2003, revised in 2006